# Two-layer stratified flows over pronounced obstacles at low-to-intermediate Froude numbers

Cecilia Cabeza,[1] Juan Varela,[1] Italo Bove,[1] Daniel Freire,[1] Arturo C. Martí,[1] L. G. Sarasúa,[1] Gabriel Usera,[2] Raul Montagne,[3,a)] and Moacyr Araujo[3]

[1]*Instituto de Física, Universidad de la República, Igua 4225, 11400 Montevideo, Uruguay*
[2]*Instituto de Mecánica de los Fluidos, Facultad de Ingeniería, Universidad de la República, CC 30, 11000 Montevideo, Uruguay*
[3]*Departamento de Oceanografía, Laboratório de Oceanografia Física Estuarina e Costeira, Universidade Federal de Pernambuco, 50740-550 Recife, Pernambuco, Brazil*

Two-layer stratified flows over abrupt topographic obstacles, simulating relevant situations in oceanographic problems, are investigated numerically and experimentally in a simplified two-dimensional situation. Experimental results and numerical simulations are presented at low-to-intermediate Froude numbers for two different obstacles: one semicylindrical and the other prismatic. In both cases, four different flow regimes downstream of the obstacles are found: (I) subcritical flow, (II) internal hydraulic jump, (III) Kelvin–Helmholtz instability at the interface, and (IV) shedding of billows. The critical values of the Froude number for the transition between different regimes depend strongly on the shape of the obstacle. In regime (III), we show that the characteristics of the lee wave that appears past the obstacle can be explained with a theoretical stability analysis. Almost independence of the vortex shedding frequency with upstream velocity is observed and explained. © *2009 American Institute of Physics*. [DOI: 10.1063/1.3110108]

## I. INTRODUCTION

The interaction between topography and stratified flows is a striking phenomena of interest for fundamental reasons and for its relevance in practical problems.[1–5] A challenging task is to quantify the characteristic features occurring at the interface of a stratified flow over an obstacle,[6–9] a situation very widespread in nature. In the atmosphere, for example, the flow around buildings or mountains is particularly important because such conditions are often related with high levels of atmospheric pollution due to low wind speeds and suppressed vertical mixing.[10–12]

In physical oceanography, the interaction of marine currents with topographic features, such as ocean banks and coastlines, result in a complex system of circulation whose characteristics are directly related to the Coriolis effect, current speed, and the size of seamounts. In this case, observational,[13–16] analytical,[17–20] numerical,[4,21,22] and previous laboratory[20,23,24] studies have suggested that the combination of streamlines splitting, current intensification, and breaking of internal lee waves, play a significant role as a mixing source in the ocean.

It is well known that seamounts enhance biological productivity and act over the ecological processes that determine the structure of local ocean life.[25,26] The rich diversity of geobiophysical scenarios has also attracted interest to understand the conditions for which generated lee waves break down and produce turbulence and vertical mixing.[27] In particular it is of interest to study mixing processes in small and coastal banks[28,29] and the influence of tides on these processes.[30]

An important number of works present systematic measurements *in situ* and a comparison with numerical models. Farmer and Armi[14] studied the role of small-scale instabilities and mixing in flow establishment at Knight Inlet sill. This fjord has a strong tidal flow which generates internal waves propagating along a pycnocline on both sides of the sill. This work led to a series of papers reporting different issues and possible explanations for them.[4,31–33] In particular, the formation of a strong downslope jet flow past the obstacle has received much attention. This phenomenon is of interest also in the atmosphere context, where this kind of jet flow is known as downslope windstorm.[10] All these works agree that larger-scale response can be sensitively dependent on small-scale instabilities.

On the other hand, in,[10] it was shown that Kelvin–Helmholtz (KH) instabilities are responsible for the wind pulsations in downslope windstorms, being three-dimensional (3D) effects of secondary relevance. We focus the present work on these instabilities, addressing an analysis of the different regimes that appear downstream near the obstacle. The effect of stratification and other parameters on the downslope jet flow was considered by Lamb,[33] maintaining the topography fixed. In this work it has been shown the influence of boundary layer separation and instabilities on the emergence of a high-drag state, and a procedure to estimate when and where flow separation can be expected was also given. Here we shall consider the influence of the obstacle shape on the jet flow and on the generation of internal waves.

Considerable efforts have been dedicated to the upstream

---

a)Present address: Departamento de Física Universidade Federal Rural de Pernambuco 52171-900, Recife, PE, Brazil.

generation of solitary waves[4,34–36] and the trapped wedge of mixed fluid behind the sill. These works show that the response of the fluid includes large-amplitude resonantly generated internal solitary waves propagating upstream. Upstream influence as a consequence of variable forcing has been also widely discussed in theoretical analysis, laboratory experiments, and numerical simulations of stratified flow.[5,31] Flow separation by a topographic obstacle and the final stage of vortex shedding in 3D orography has also received attention.[31,32,37] Note that in our setup, in contrast to Ref. 37 where vortex shedding is a consequence of the three dimensionality of the flow, the dynamics is two dimensional.

Analytic theories for lee waves and hydraulic jumps usually assume that flow separation does not occur.[1] However, under suitable conditions the mainstream ceases to flow approximately parallel to the obstacle beyond a certain point causing the phenomenon of separation and flow reversion.

In a similar way to the theoretical analysis, experimental investigations studying the interaction between stratified flows and topography are also mostly limited to the cases in which the bottom surface is smooth.[1,6,24] However, in a few exceptions the role of abrupt obstacles is investigated. For example, in the work of Aguilar and Sutherland[9] the generation of internal waves by different periodic abrupt topography is investigated. They showed that internal waves are generated not only by flow over the hills but also by flow over boundary-trapped lee waves and vigorous turbulence created in the lee side of sharp-crested hills. Thus, it is of interest to go deeper into the mechanisms of mixing over abrupt obstacles in stratified flows.

The present paper compares experimental and numerical results in the case of isolated abrupt obstacles, with those obtained from hydraulic theories for smooth obstacles in order to test their range of applicability. The experiments were performed in such a way that the flow could be assumed two dimensional. We used two layers of different densities, with constant density inside each layer. In a previous work[38] we studied numerically and experimentally the different instabilities developed in a two-layer stratified flow over a pronounced obstacle. Here, we extend this previous work to two-layer flows over prismatic and semicylindrical abrupt obstacles focusing on the role of the geometry, flow separation and mixing mechanisms.

This paper is organized as follows. In Sec. II we briefly review the treatment of two-layer flows using hydraulic theory. In Sec. III we present the experimental setup. The numerical simulations are given in Sec. IV. The results obtained from the experiments and simulations and their comparison are given in Sec. V. In Sec. VI we present the results of linear stability analysis of the flow past the obstacle. Finally, a summary and the conclusions are given in Sec. VII.

## II. HYDRAULIC THEORY OF A TWO-LAYER FLOW PROBLEM

Let us consider a linear theory for a flow consisting of two layers of different densities $\rho_1$ and $\rho_2 (\rho_2 > \rho_1)$ over a fixed obstacle. Throughout this paper, subindices 1 and 2 correspond to the upper and lower layers, respectively. We
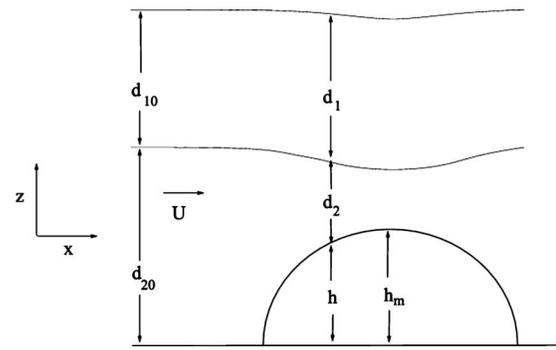


FIG. 1. Sketch showing variables used in the description of the two-layer flow. $\vec{U}$ is the upstream uniform fluid velocity, $d_1$, $d_2$ are the depth of the layers, and $h$ is the height of the obstacle at a given location with $h_m$ the maximum height of it.

define a Cartesian reference frame with coordinates $(x, y, z)$, where the flow is in the $x$ direction and $z$ is directed vertically upward. As mentioned in Sec. I, we shall focus on situations where variations in the $y$ direction can be neglected and the problem can be considered two-dimensional. The depths of the layers are functions of $x$, as their thicknesses depend on the position where measured. Thus, the depth of the upper and lower layers are $d_1(x)$ and $d_2(x)$, respectively, and the height of the obstacle is $h(x)$, as sketched in Fig. 1. Far upstream, the depths are named $d_1(x=0) = d_{10}$ and $d_2(x=0) = d_{20}$.

The mean velocities of the fluid in each layer are $u_1$ and $u_2$. Let us assume that the fluid velocity is uniform far upstream, with $u_{10} = u_{20} = U$. In addition, we assume: (a) the pressure is hydrostatic, (b) Boussinesq approximation, which implies that $\epsilon = (\rho_2 - \rho_1)/\rho_2 \ll 1$, is valid, and (c) the top boundary of the upper layer is a free surface at constant pressure $p_s$, taken to be $p_s = 0$. The flow over the topography is then characterized by the densities $\rho_1$, $\rho_2$, the depth of the layers $d_1$, $d_2$, the mean velocity in each layer $u_1$, $u_2$, and the height of the obstacle $h$. With these assumptions, Bernoulli functions for each layer may be written as

$$E_1 = \rho_1 g(d_2 + d_1 + h) + \tfrac{1}{2}\rho_1 u_1^2,$$

$$E_2 = \rho_1 g d_1 + \rho_2 g(d_2 + h) + \tfrac{1}{2}\rho_2 u_2^2. \tag{1}$$

Following Lawrence's model,[6,7] from the conditions $dE_i/dx = 0$ and imposing mass conservation in each layer the following relation is obtained:

$$\frac{(1 - F^2)}{\epsilon F_1^2 F_2^2} \frac{dD}{dx} = \frac{dh}{dx}, \tag{2}$$

where $F^2 = F_1^2 + F_2^2 - \epsilon F_1^2 F_2^2$ is the composite internal Froude number while $F_i^2 = u_i^2/(g'd_i)$ $(i = 1, 2)$ are the Froude numbers for each layer with $g' = [1 - (\rho_1/\rho_2)]g$, and $D = d_1 + d_2 + h$. It has been shown[6] that $F$ is the adequate composite Froude number for characterizing a two-layer flow; i.e., if $F > 1$ the flow is internally supercritical (the internal small waves cannot propagate upstream against the background flow), and if $F < 1$ the flow is subcritical (the disturbances may propagate in both directions). When $F = 1$, the flow is termed critical

and this location is usually called a control point. The transition from subcritical to supercritical flow is of special interest in our experiments. When the flow is supercritical, an internal hydraulic jump which is an important source of turbulence and mixing may take place. From Eq. (2), it follows that the critical condition $F=1$, may occur if $dh/dx=0$. For that value of $F$, when the surface has horizontal tangent, i.e., at the crest of the obstacle, the flow undergoes a transition from subcritical to supercritical. If, in addition, the condition $\epsilon \ll 1$ is imposed (which is satisfied in our experiments), the composite Froude number may be expressed as $F^2=F_1^2+F_2^2$. On the other hand, in the present study we consider flows where $F_i^2 \lesssim 1$. Thus, from Eq. (2) and the Boussinesq approximation it follows that

$$\frac{dD}{dx} = \frac{\epsilon F_1^2 F_2^2}{1-F^2}\frac{dh}{dx} \approx 0. \tag{3}$$

Therefore, we consider $D=d_{10}+d_{20}$ a constant. Hence the free surface will be taken as horizontal.

In order to obtain the critical values of the flow parameters for the subcritical-supercritical transition, we impose that $E_2-E_1$ is constant and, using the Boussinesq approximation, we obtain

$$\frac{1}{2}r(1-r)F_0^2\left(\frac{r_0^2}{r^2} - \frac{(1-r_0)^2}{(1-r_0H-r)^2}\right) + r_0(H-1) + r = 0, \tag{4}$$

where $r=d_2/D$, $r_0=d_{20}/D$, $H=h/d_{20}$, and

$$F_0 = \sqrt{\frac{U^2}{g'd_{10}} + \frac{U^2}{g'd_{20}}} \tag{5}$$

is the Froude number $F$ calculated in the upstream flow far from the obstacle. We shall call $F_0$ as the global Froude number. On the other hand, the critical condition $F^2=1$ may be expressed as

$$r(1-r)F_0^2\left(\frac{r_0^2}{r^3} + \frac{(1-r_0)^2}{(1-r_0H-r)^3}\right) = 1. \tag{6}$$

Thus, Eqs. (4) and (6) imposed at the crest of the obstacle may be used to determine, $F_{0c}$, the critical value of $F_0$ for the occurrence of supercritical flow. In our experiments we fixed the aspect ratio $r_0=0.6$, and we considered different values of $H_m=h_m/d_{20}$, $h_m$ being the height of the obstacle. The critical values, $F_{0c}$, for the occurrence of critical flows as a function of $H_m$ are obtained solving Eqs. (4) and (6). The results are shown in Sec. V, Fig. 7 where they are compared to the experimental results.

Theoretical solutions for the flow when $F_0$ is larger than $F_{0c}$, i.e., when the flow is beyond the critical condition, have been obtained in Refs. 1 and 7. These solutions predict a range of $F_0$ values for which there is a wave moving backward to the flow changing the conditions upstream. These approaches allow the calculation of the velocity and amplitude of this wave. This type of wave has been also obtained using the Korteweg–de Vries equation including quadratic and cubic nonlinearity,[3] and numerical simulations, with steplike stratification[36] and linearly varying stratification.[34]
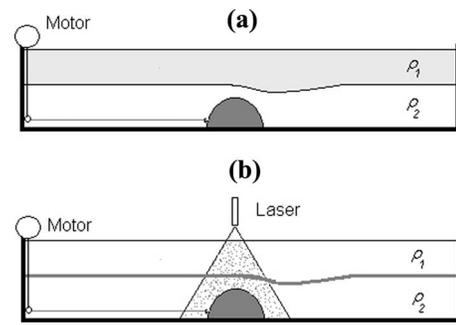


FIG. 2. Schematic of the experimental configuration and the two visualization techniques used. (a) The upper layer is dyed with $KMnO_4$ to obtain good contrast for visualization when the tank is lighted from behind. (b) The DPIV is carried out lightening from above with a laser. In this case, in order to distinguish the interface, only a thin portion of the upper layer is dyed.

For Froude numbers clearly exceeding the critical condition, experiments inside a container may be difficult due to accumulation of wave effects on one edge of the tank. Consequently, this provokes grater thickness of the layers than those obtained in an unlimited flow. This effect is more important the greater the $F_0$ is. For instance, from the theory[1] follows that for $F_0=0.181$, $r_0=0.6$, and $H_m=0.833$, the increment of the thickness is significant, $d_{10}'/d_{10}=1.10$, where $d_{10}'$ is the thickness of the interface taking into account the effects of the upstream wave. On the other hand, for $F_0=0.11$, $d_{10}'/d_{10}=1.03$, the effects of this wave are negligible. Since for $H_m=0.833$ and $r_0=0.6$, the critical value is $F_{0c}=0.06$, we can moderately exceed this value without significant distortion of the upstream wave. Thus, quantitative good results may be obtained within a broad range of parameter values.

## III. EXPERIMENTAL SETUP

Our experiments were performed in a water tank of size equal to $2.0 \times 0.29 \times 0.137$ m$^3$. We used a closed channel where we towed the obstacle at different velocities with a calibrated motor (Fig. 2). The velocities of the fluid referred to a reference frame fixed to the obstacle. In our previous work,[38] we showed that this configuration is equivalent to the flow over a fixed obstacle. Moreover, we only focused our observations on the central region of the tank where the structures are persistent and the far boundary effects can be neglected. In this work, we always show images and diagrams of leftward moving obstacles.

We used two different obstacle shapes, prismatic and semicylindrical, both of them with height of $h_m=0.125$ m, width of $W_0=0.13$ m, and length of $L=0.25$ m, see Fig. 3. The obstacles were scaled in such a way that the confinement aspect ratio verifies $W_0/W \lesssim 1$ ($W=0.137$ m, width of the water tank) and the lateral flow around the obstacle can be neglected in order to reduce the problem to a quasi-two-dimensional situation.

As mentioned above, we want to create a density profile with an abrupt gradient at the interface. In order to get this steplike stratification we first filled the tank with a layer of density $\rho_2=1002$ kg/m$^3$ using NaCl solution. To fill the upper layer, pure water with density $\rho_1=1000$ kg/m$^3$ was care-
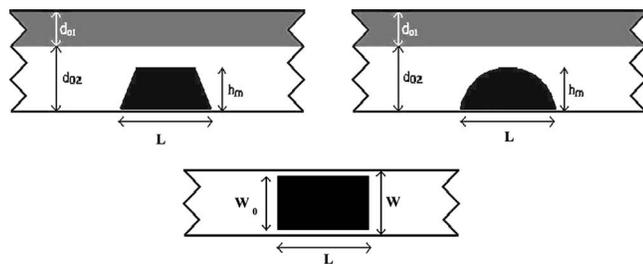
FIG. 3. Side (top) and plan view (bottom) of the prismatic and semicylindrical obstacles, where $d_{10}$, $d_{20}$ are the depth of the layers, $h_m$ is the maximum height, and $L$ is the length of the obstacle. $W$ is the width of the water tank and $W_0$ the width of the obstacle.

fully poured over a sponge floating on the free surface. The time scale of the molecular diffusion between the layers is much longer than the typical experimental times. Despite that, due to the mixing produced by the moving obstacle, after a few measurements, the tank had to be emptied and new fluid layers poured in again.

The flow was examined via two standard techniques: dye visualization and digital particle image velocimetry (DPIV). In the first case, the upper layer was dyed with $KMnO_4$ solution in order to obtain a good visual contrast between both layers. A powerful source of fluorescent light from behind was used to obtain a uniform illumination. We obtained global qualitative pictures of the flow with this technique. In the second case, DPIV allows us to obtain quantitative values of velocity field based on the cross correlation of two consecutive images recorded by a digital camera. Neutrally buoyant polyamide particles of $50 \times 10^{-6}$ m diameter were seeded in the bottom layer. A green laser sheet of 100 mW is used to illuminate a cross section plane of the flow which is recorded by a digital camera PIXELINK PL-A741. In order to control the interface and avoid attenuation of the laser light as much as possible, when using this technique, only a thin layer of water at the bottom of the upper layer is dyed.

For both obstacle shapes, five different sets of heights were chosen always keeping constant the characteristic ratio $r_0 = 0.6$. The experiment was repeated for each set of heights with a wide range of velocities analyzing the different behaviors, using the two visualization techniques mentioned above.

## IV. NUMERICAL METHOD

The numerical simulations considered here were obtained with the in-house flow solver CAFFA3D.MB (Ref. 39) developed jointly by Universitat Rovira i Virgili (Tarragona, Spain) and Universidad de la República (Montevideo, Uruguay). It is an original FORTRAN95 implementation of a fully implicit finite volume method for solving the 3D incompressible Navier–Stokes equations in complex geometry using block structured grids. This 3D solver, based on a previous two-dimensional solver,[40] is described and validated in Refs. 41 and 42.

The unsteady incompressible Navier–Stokes equations with Boussinesq approximation for buoyancy terms were considered. Since the Reynolds number was below Re

$=1.10^3$ for all cases, no turbulence model was required and transient solutions were computed directly. The time step was set to $2.0 \times 10^{-2}$ s for all cases. This time scale is about $(h_m/U)/10^3$ for the highest velocity case. Simulations were run starting from null-velocity fields through $10^4$ time steps, or about 200 s of flow time.

In the simulations, the obstacle remains fixed against a steady two-layer current of fluid. Thus a uniform velocity profile was specified at the upstream boundary located at a distance of $8h_m$ upstream from the obstacle, and a null gradient outlet was used at the downstream boundary, located $15h_m$ downstream. As the top surface is not disturbed by the flow, it was modeled as an horizontal slip boundary at fixed height. All other boundaries correspond to wall surfaces. Nonslip condition was directly applied to them, including the vertical walls of the channel. Hence, the simulation accounts fully for 3D effects, although the flow reveals itself as essentially two dimensional due to the geometry of the obstacles and the relatively low Reynolds numbers.

For both obstacles the grid was made up of three blocks, although the topology was different in each case. For the prismatic obstacle, three straight blocks were assembled with two at each side of the obstacle and the third extending on top of them along the domain. On the other hand, for the cylindrical obstacle one C-grid block was used around the obstacle together with two other straight blocks, upstream and downstream of the obstacle.

Grid resolution was set essentially uniform through the domain at $h_m/25$, being enough to resolve flow details at these rather low Reynolds numbers. Due to the layout of the grid in the cylindrical obstacle case the spatial resolution normal to the wall was slightly higher near the obstacle, reaching about $h_m/35$.

## V. RESULTS

Let us start this section by discussing the different regimes observed in the experiments and simulations. Using the dye technique we visualized the different regimes as a function of the obstacle velocity and the aspect ratio. In Figs. 4 and 5, we show experimental and numerical results for the prismatic and semicylindrical obstacle with $r_0 = 0.6$, $H_m = 0.833$, and different values of $F_0$. In all the considered experiments, the upstream flow is subcritical, i.e., $F_0 < 1$. In these figures we distinguish four regimes, all of them present in both obstacles. However, both experimental and numerical results reveal a very important point: the regimes begin at different critical Froude numbers for different geometries. In spite of relatively small quantitative differences, the numerical and experimental results for both topographic shapes show a qualitative similarity.

Regime (I), Figs. 4(a) and 5(a), corresponds to situations in which the flow is subcritical, $F < 1$, everywhere over the obstacle. At low velocity, we observe that a jet through the bottom layer develops near the obstacle. As the velocity is increased, the jet begins to separate from the obstacle and rises horizontally. A transition from regime (I) to (II), Figs. 4(b) and 5(b), occurs when the local Froude number reaches a control point ($F = 1$) somewhere over the obstacle. Regimes

Experimental          Numerical
Fo = 0.035                (a)

Fo = 0.047                (b)

Fo = 0.111                (c)
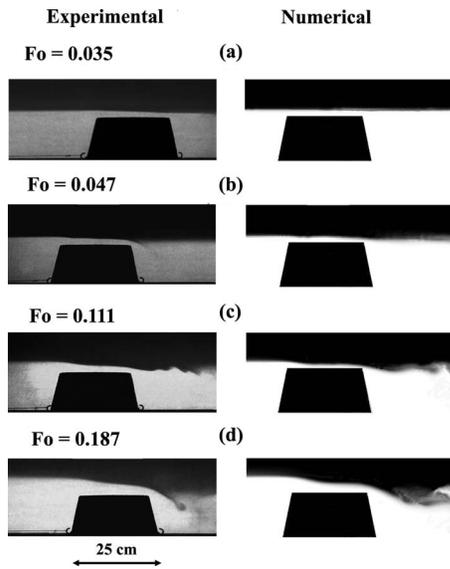
Fo = 0.187                (d)

25 cm

FIG. 4. Experimental snapshots (left) and numerical simulations of a flow (right) past an prismatic obstacle corresponding to the different regimes, for $r_0$=0.6 and $H_m$=0.833. (a) Subcritical regime (i). (b) Internal hydraulic transition (II). (c) KH instability at the interface (III). (d) Billow formation (IV). In all the images the values of the Froude numbers $F_0$ are indicated on the labels.

Experimental          Numerical
Fo = 0.039                (a)

Fo = 0.053                (b)

Fo = 0.072                (c)
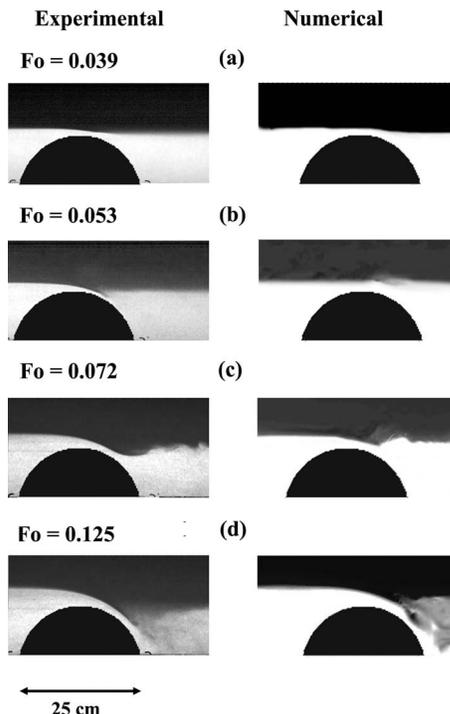
Fo = 0.125                (d)

25 cm

FIG. 5. Experimental snapshots (left) and numerical simulations of a flow (right) past a semicylindrical obstacle for the different regimes. (a) Subcritical regime (i). (b) Internal hydraulic transition (II). (c) KH instability at the interface (III). (d) Billow formation (IV). Same parameters as in Fig. 4.
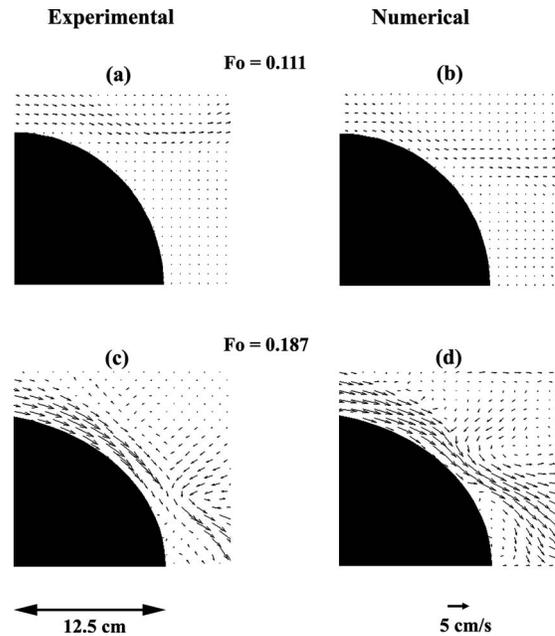
Experimental          Numerical
Fo = 0.111
(a)                       (b)

Fo = 0.187
(c)                       (d)

12.5 cm                    5 cm/s

FIG. 6. Comparison between experimental (left) and numerical (right) results for semicylindrical obstacle. Top row $r_0$=0.6 and $F_0$=0.111. Bottom row $r_0$=0.6 and $F_0$=0.187.

(II) and on are all supercritical past the obstacle. As a consequence, an internal hydraulic transition develops at the lee side. The interface between the layers is smoothly disturbed both in regimes (I) and (II). However, an intense jet is developed at the lee side. When the velocity gradient around the jet is strong enough, KH instability appears inside the lower layer.

Increasing the Froude number $F_0$ further we reach regime (III), Figs. 4(c) and 5(c), where a clearly visible lee wave perturbs the interface separating the two layers with a quasisinusoidal profile. This perturbation, as we show in Ref. 38 and we will demonstrate in Sec. VI, is produced by KH instability when the jet arrive to be horizontal enough to produce a substantive difference in the velocity of the fluid at both sides of the interface. Downstream, a secondary instability develops mixing is observed. Finally, regime (IV), Figs. 4(d) and 5(d), is characterized by the shedding of vortical portions of lighter fluid which are separated from the upper layer. As a consequence, intense mixing between the two layers takes place. In this regime, the interface between both layers is strongly disturbed. The jet drags fluid from the upper layer and shedding of billows take place. A peculiar characteristic of this shedding is the frequency of the vortical billows which is almost constant in respect to variation in the velocity $U$. To the best of the authors' knowledge, this type of vortex shedding has, hitherto, been unreported.

Numerical results are in good agreement with experimental results, as can be visualized in Figs. 4 and 5. The regimes observed in the experiments were also obtained in the numerical simulations for the two obstacles that were used. The overall agreement between numerical and experimental method can be also seen in Fig. 6, corresponding to regimes III and IV.

However, as $F_0$ gets well above the critical value $F_{0c}$ (regime IV, vortex shedding), numerical and experimental results begin to differ. For the prismatic obstacle, vortex shedding starts earlier in experiments than in the simulations [Fig. 4(d)]. Whereas in the cylinder case the numerical simulations show vortex shedding before experiments do so [Fig.
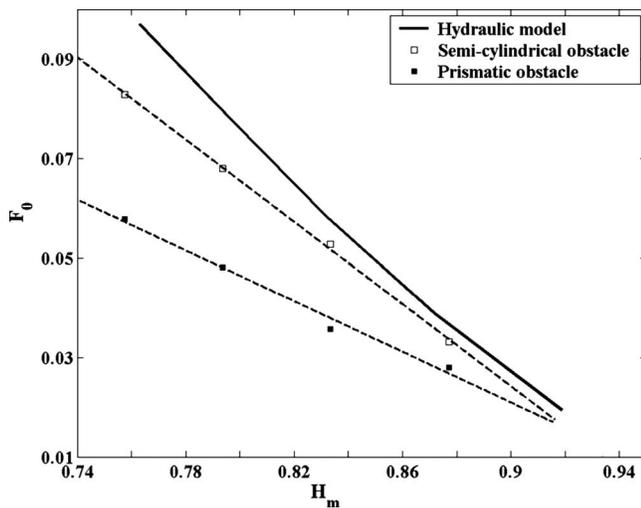
FIG. 7. Critical global Froude number as a function of the aspect ratio $H_m$, for a fixed relation between the height of the layers $r_0=0.6$. The continuous line corresponds to the hydraulic model and the symbols to the experimental results of the two obstacles considered: semicylindrical (open squares) and prismatic (full squares).
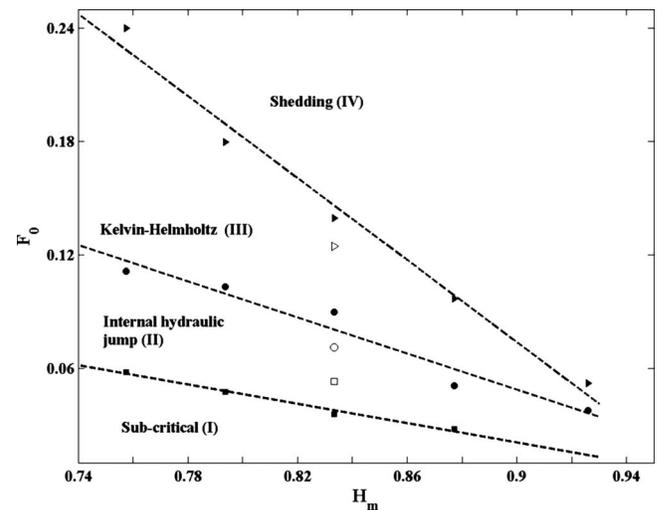


FIG. 8. Stability diagram of the different regimes for the prismatic (full symbols) and the semicylindrical (open symbols) obstacle as a function of the global Froude number $F_0$ and the aspect ratio $H_m$ for $r_0=0.6$. Dotted lines are linear approximations of those experimental points. Squares correspond to the transition between subcritical to internal hydraulic jump regimen. Circles correspond to the onset of KH regimen. Triangle symbol correspond to the onset of shedding of billows regimen.

5(d)]. We attribute these differences to the effect of the upstream moving wave. This point will be discussed below.

In Fig. 7 we show the global Froude number $F_0$ as a function of the aspect ratio $H_m$ for the transition from subcritical to supercritical flow. The continuous line corresponds to the theoretical global Froude number for a smooth obstacle as it was calculated solving Eqs. (4) and (6). The experimental $F_0$ is represented by open squares for the semicylindrical obstacle and with filled squares for the prismatic one. The dashed lines are the linear fitting of the experimental points. This graph clearly reflects the fact that the smoother the obstacle, the higher the velocity that will be needed to reach the critical Froude number. Then, the critical values for the semicylindrical obstacle are located between the values of the prismatic obstacle and the theoretical prediction (valid for a very smooth obstacle). In this way, with laboratory experiments, we prove that the transition from one regime to another strongly depends on the geometry of the obstacle. Hence, given an upstream flow, the flow downstream may be subcritical or supercritical, depending on the geometry of the obstacle.

In order to establish the transition between different regimes, we use DPIV technique. With the measured velocity field we determine if the flow attained the critical point $F=1$. A stability diagram is presented in Fig. 8, showing the different regimes as a function of the global Froude number $F_0$ and the aspect ratio $H_m$, for $r_0=0.6$. The diagram shows the transition values between the regimes for the prismatic obstacle (full symbols) and semicylindrical obstacle (open symbols). The dotted curves are guides for the eyes. We also show the transitions between the different regimes with the cylindrical obstacle for $H_m=0.833$ (open symbols, see details in the figure caption). It is interesting to note that although the prismatic obstacle reaches the supercritical regime at a lower velocity than the semicylindrical obstacle, KH develops at higher velocities than in the case of the semicylindrical obstacle.

The slope of the jet after the obstacle plays an important role in the transition between the different regimes. Indeed, it was observed that transition depends not only on $F_0$, $r_0$, and $H_m$ but also in the shape of the obstacle, i.e., the slope of the jet after the obstacle. As a result, the lee waves past the prismatic and semicylindrical obstacles have similar characteristics at different Froude numbers. We exemplified this in Fig. 9 where we show KH instability at the interface for the two obstacles. Although the prismatic obstacle reaches the supercritical regime at a lower velocity than the semicylindrical obstacle, for the prismatic obstacle KH develops at higher velocities than in the case of the semicylindrical obstacle. This is due to the abrupt geometry of the prismatic bank, in which the jet flow needs higher velocity to rise up and develop KH.

As already mentioned, we characterized the velocity profiles via DPIV analysis. Figure 10(b) shows the visualization of the velocity profile over the semicylindrical obstacle obtained with DPIV technique at the places indicated in Fig. 10(a). We observe that the shape of the jet is nearly triangular and quite constant at different distances from the obstacle. These results will be used to make an hydraulic stability analysis of the interface (see Sec. VI).



FIG. 9. Flow passing over the two obstacles of different geometry. These snapshots correspond to the KH instability between both layers at $F_0=0.102$ for the prismatic obstacle and at $F_0=0.064$ for the semicylindrical obstacle.
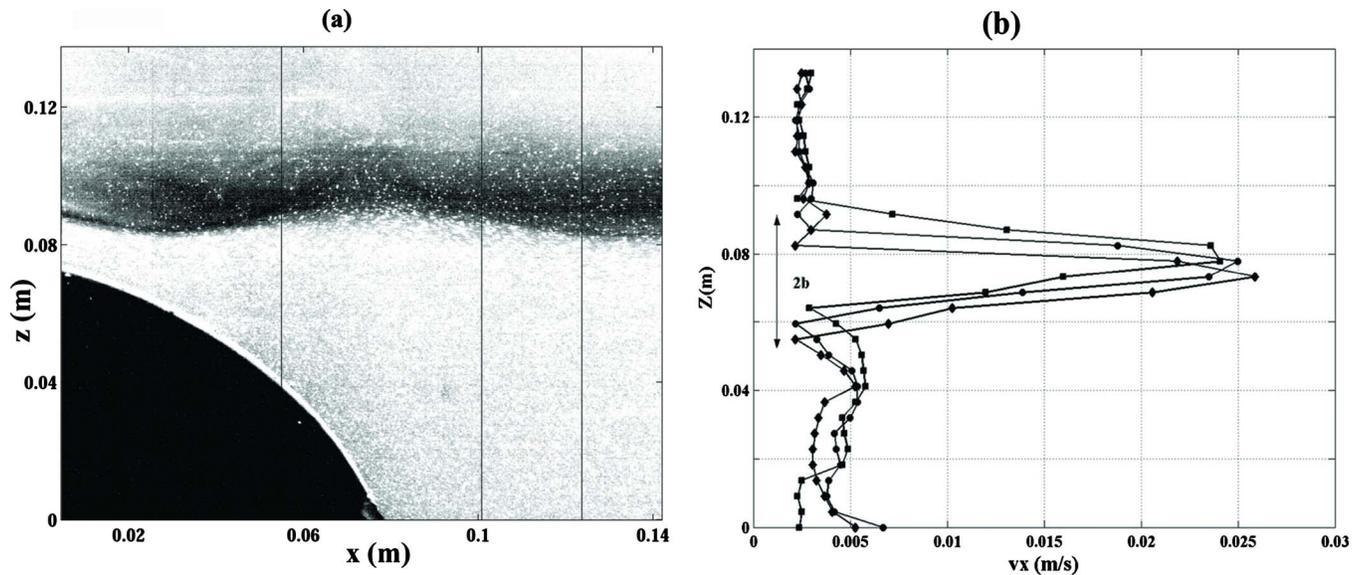
FIG. 10. (Color online) (a) DPIV image for the semicylindrical obstacle for KH instability at $F_0=0.122$. The vertical lines correspond to the places where the velocity profiles were taken. (b) Velocity profiles for the three positions marked in the image displayed in (a).

In regime III as the flow velocity $U$ is increased, the inclination of the jet, the amplitude of the interface wave, and the velocity of the jet increase. However, when the Froude number exceeds the critical value, the wave at the interface is no longer observed and the flow enters in regime IV. In this regime, there is shedding of vortical portions of the lighter fluid which submerge into the lower layer.

The shedding of billows in regime (IV), as can be seen in Fig. 11, could also be caused by KH instability. In order to test this hypothesis, we correlated the thickness of the jet $a$ and the distance between the billows $x_b$. If the shedding is caused by KH instability, the distance between the billows must be approximately the wavelength of the most unstable mode. Table I shows the values of $a$ and $x_b$ and the ratio between them for cases $r_0=0.6$ and $H_m=0.83$, for the prismatic obstacle at different velocities. These results reveal a

clear proportionality between $a$ and $x_b$, with a slope of $x_b/a=2.7$. Indeed, in Sec. VI we consider a triangular jet, and we show that the dimensionless wave-number of the most unstable mode is given by $kb=1.225$. Then, the ratio between the corresponding wavelength and the thickness of the jet $a$ ($a=2b$) is given by $\lambda/a=2.57$, which is in very good agreement with the ratio (2.6–2.7), obtained experimentally.

As commented in Sec. II theoretical solutions based on hydraulic theory predict that for $F_0>F_{0c}$, there is a wave that propagates in opposite sense to the flow, modifying the upstream conditions. The role of this upstream wave has been deeply studied theoretically, observationally, and numerically.[4,14,31,33]

In order to study the effect of this upstream wave in our results, we performed numerical simulations, in a broad range of values of the $F_0$, focusing on the dynamics far upstream the obstacle and looking for the transitory effects. Temporal evolution of the upstream wave, for $F_0=0.35$, is shown in Fig. 12. We note that the profile of the upstream wave is very smooth. This is in contrast with the hydraulic theory, which considers that the upstream wave has a discontinuity. As already mentioned, accumulation of wave effects in the closed container for Froude numbers clearly exceeding the critical condition produces that the thicknesses of the layers are larger than those obtained in an unlimited flow.
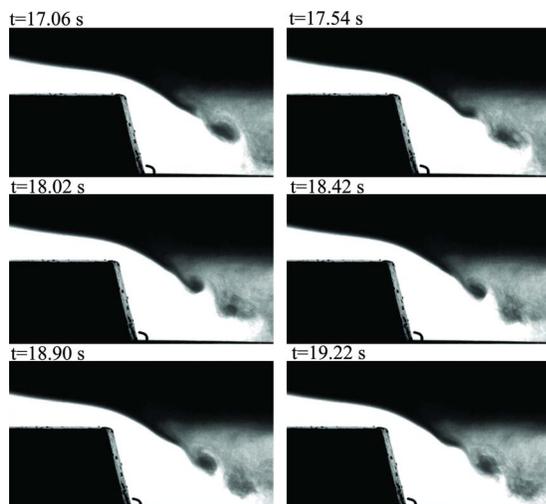


FIG. 11. (Color online) Shedding of billows for $H_m=0.76$, $r_0=0.6$, and $F_0=0.26$ for the prismatic obstacle. The frequency of shedding is 0.5 s$^{-1}$. The wavelength is the same of the KH.

TABLE I. Thickness of the jet $a$ and distance between the billows $x_b$ for $r_0=0.6$ and $H_m=0.83$.

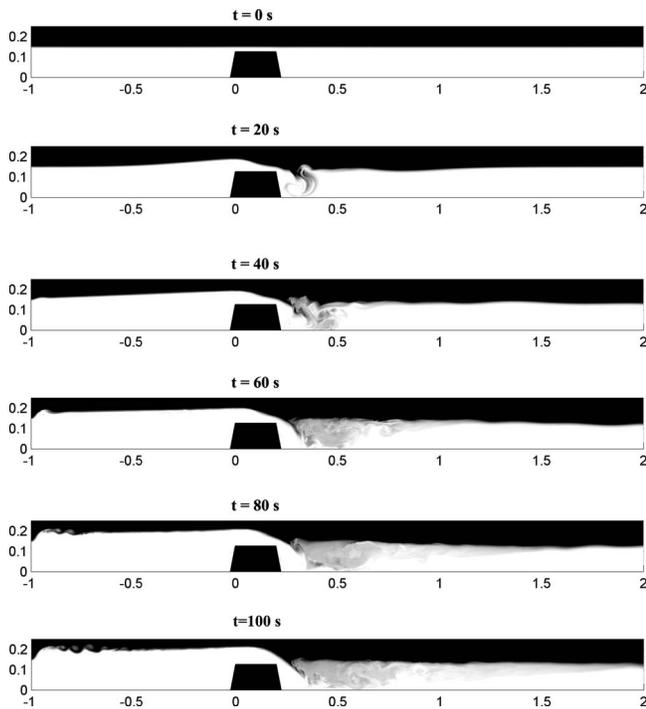| $U$ (cm/s) | $a$ (cm) | $x_b$ (cm) | $x_b/a$ |
|---|---|---|---|
| 0.45 | 2.1 | 5.4 | 2.6 |
| 0.55 | 2.3 | 6.2 | 2.7 |
| 0.65 | 2.8 | 7.4 | 2.6 |

FIG. 12. Transient evolution of the interface showing the upstream influence of the wave corresponding to $F_0=0.35$. The simulations start at $t=0$ with a null-velocity condition.

Furthermore we note that the results in Figs. 7 and 8 for $F_0 < 0.11$ are not distorted in any way by the upstream effect. In the region $F_0 > 0.11$ although the results could be slightly distorted, they remain qualitatively correct as we can conclude from comparison with the numerical simulations.

## VI. STABILITY ANALYSIS OF THE JET PAST THE OBSTACLE

As described in Sec. V, in the lee side of the obstacle the flow presents different regimes depending on the values of $F_0$, $r_0$, and $H_m$. However the type of flow downstream is not only determined by the flow parameters but also by the slope of the jet past the obstacle. We will analyze the stability of this flow.

In regime III, the interface between the two layers is perturbed by a quasisinusoidal wave, which breaks down when its amplitude is sufficiently large, indicating that a secondary instability takes place. DPIV measurements clearly show that the jet is located near the interface, and we conjecture that this wave results from a primary KH instability. We test this hypothesis based in the experimental measures shown in Fig. 10(b) and we will describe the flow near the interface as a triangular jet. The flow is given by

$$V = \begin{cases} V_1, & \text{for } z > b \text{ and } z < -b \\ V_2 + (V_1 - V_2)|z|/b, & \text{for } -b < z < b, \end{cases} \quad (7)$$

where $2b$ is the thickness of the jet and the densities are $\rho_2$ for $z < b$ and $\rho_1$ for $z > b$. We perform standard linear stability analysis assuming a stream function of the perturbations $\psi$ of the form[43,44]
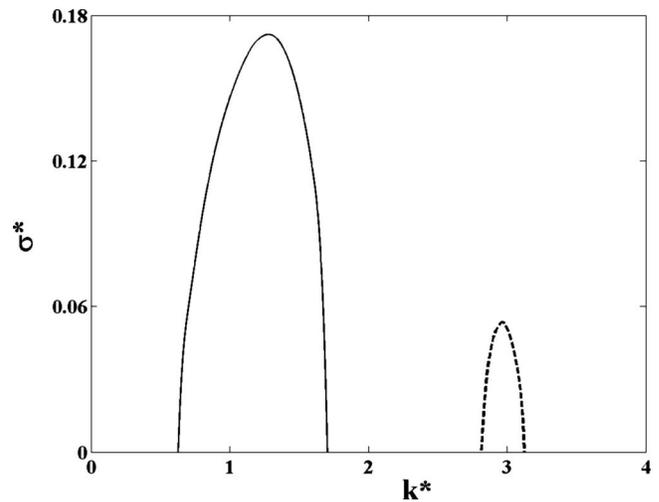


FIG. 13. Nondimensional growing rate of the perturbations for the unbounded stratified jet (continuous line) and the stratified jet near a wall (dashed line), defined by Eqs. (7) and (12), where $k^*=kb$ and $\sigma^*=\sigma b/(V_2-V_1)$.

$$\psi(x,z,t) = \phi(z)\exp[ik(x-ct)], \quad (8)$$

where $\exp[ik(x-ct)]=\exp[ik(x-c_r t)]\exp \sigma t$, with $\sigma=kc_i$, and $c_i, c_r$ are the imaginary and real parts of the phase velocity $c$, respectively. Thus, $\sigma$ represents the growing rate of the perturbations. If $\sigma > 0$, then the flow is unstable to these perturbations, and if $\sigma < 0$ the flow is stable. Since the flow under consideration has constant density in each layer, $\phi(z)$ is determined by Rayleigh's equation

$$\phi''(z) - k^2\phi(z) = 0, \quad (9)$$

whose general solution is $\psi_i(z)=A_i \exp(kz)+B_i \exp(-kz)$, where the index $i=1,2,3,4$ denotes the solution for the regions $z > b$, $b > z > 0$, $0 > z > -b$, and $z < -b$, respectively. The perturbations must be bounded at $z \to \infty$ and $z \to -\infty$, then the $\phi_i$'s become

$$\phi_1(z) = B_1 \exp(-kz),$$

$$\phi_2(z) = A_2 \exp(kz) + B_2 \exp(-kz),$$

$$\phi_3(z) = A_3 \exp(kz) + B_3 \exp(-kz), \quad (10)$$

$$\phi_4(z) = A_4 \exp(kz).$$

We now impose the boundary conditions across the limits separating the regions by requiring continuity of vertical velocity and pressure. Since the velocity profile is continuous, the first of these conditions is equivalent to require $\phi_i(z_j)=\phi_{i+1}(z_j)$,[44] where $z_j$ denotes the position of the boundary that separates regions $i$ and $i+1$. The second of these conditions requires

$$(U_i(z_j) - c)\phi'(z_j)_i - U_i'(z_j)\phi_i$$
$$= (U_{i+1}(z_j) - c)\phi'(z_j)_{i+1} - U_i'(z_j)\phi_{i+1}. \quad (11)$$

The boundary condition yield a linear system of equation on $(B_1, A_2, B_2, A_3, B_3, A_4)$. The dispersion relation, i.e., the relationship between $k$ and $c$, is obtained discarding the

trivial solution. The numerical results obtained by solving the dispersion relation are shown in Fig. 13. The normal modes stability analysis gives that the more unstable mode corresponds to the wave number $k=1.225/b$. For $b=1.1$ cm [see Fig. 10(b)], the corresponding wavelength is $\lambda=10.3$ cm which is in good agreement with the experimental data of $\lambda=10.2$ cm. We also performed the linear stability analysis of a jet that is located near the wall of the obstacle, with field velocity given by

$$V = \begin{cases} V_1, & \text{for } z \geq b \\ V_2 + (V_1 - V_2)|z|/b, & \text{for } -b < z < b, \end{cases} \quad (12)$$

where the rigid boundary is located at $z=-b$, and the densities are $\rho_2$ for $z<b$ and $\rho_1$ for $z>b$. In this case, we have three regions with corresponding stream functions $\phi_1(z)$, $\phi_2(z)$, $\phi_3(z)$. The condition at the rigid boundary is given by $\phi_3(-b)=0$,[44] and the other boundary conditions are the same as the ones imposed for the unbounded jet. From this analysis we obtained that the jet is partially stabilized in the proximity of the wall of the obstacle, that is, the instabilities grow slowly compared to the unbounded case (Fig. 13). This result is in agreement with those obtained previously by Hazel.[45] This stabilizing effect is caused by the combination of the density stratification and the presence of the wall. Then the wall has little effect on the stability of the jet if the density is constant. This explains why the instabilities appear downstream, but not over the obstacle, where the jet is located on a rigid boundary. The stability analysis results and the measured wavelength of the lee waves in regimes III and IV, strengthen the assumption that the instabilities observed past the obstacle in both cases are caused by KH instability.

We can also explain the fact that the frequency of the billows is almost independent of the velocity $U$. From Table I we can see that the thickness of the jet is (for fixed $r_0$ and $H_m$) practically proportional to $U$. The frequency of the billows can be expressed as $f=x_b/u_b$, where $u_b$ is the velocity of the billows. Since $x_b$ is nearly proportional to $U$, if we assume that $u_b$ is proportional to $U$, then the frequency is weakly dependent on the velocity $U$. This is in contrast with vortices produced in flows such as Von Karman's street, where the frequency, in a wide velocity range, is almost proportional to the velocity. The difference resides in the fact that in Von Karman's flow, the characteristic length is constant (the diameter of the cylinder), while here the characteristic length (the thickness of the jet) varies almost proportional with $U$, which causes that the wavelength of the most dangerous mode increases with $U$. This effect compensates the increasing of $u_b$ with $U$, leaving the frequency almost constant.

## VII. SUMMARY AND CONCLUSIONS

We studied two-layer stratified flows over abrupt obstacles (prismatic and semicylindrical shapes) focusing on the effects of the geometry and the generation of disturbances and correlated mixing. Although this type of bottom surface may appear in real situations, the problem has received little attention in literature. We performed measurements of the velocity fields with DPIV technique and studied the stability of the obtained profiles. It is remarkable that in all cases which we studied, the critical value of the global Froude number, $F_{0c}$, was less than that predicted by the hydraulic theory, which is valid for smooth varying bottom surfaces. This result indicates that an abrupt obstacle reaches the control point for lower velocities than for a smooth obstacle. In other words, for a given $F_0$, a flow that is subcritical for a certain geometry could be supercritical for another geometry. As could be expected, as a consequence of its smoother geometry, the results for the semicylindrical obstacle are closer to the hydraulic theory than those of the prismatic obstacle. Despite the fact that the conditions are far from those required for the hydraulic theory to be valid, we found that this theory still allows us to estimate accurately the thickness and average velocity of the strong jet that forms past the obstacle. However, the presence of flow separation and dissipation, at the lee side of the obstacle, prevents the use of hydraulic theory from making further predictions.

As regard the downstream flow, four different regimes were identified and represented in parameter space $F_0-H_m$. In regime I the flow is subcritical everywhere, while in regime II and all the subsequent regimes, the flow past the obstacle is supercritical. The beginning of regime II was determined calculating the local Froude number with the velocity fields experimentally measured. In this regime, a shear instability develops mainly in the lower layer. The interface that separates the layers is disturbed by a quasisinusoidal wave in regime III. We demonstrate that this disturbance is originated by KH instability. Hence, the jet that forms past the obstacle controls the dynamics of the lee side flow. Furthermore, this quasisinusoidal wave disturbance breaks down through a secondary instability for sufficiently large amplitude and departure from two dimensionality takes place. Regime IV exhibits strong mixing caused by the shedding of billows. An interesting fact is that the frequency of the billow generation is almost independent of the velocity $U$. A stability analysis on the jet immediately after the obstacle allowed us to verify that the mechanism leading to vortex shedding was also produced by KH instability. The distance between the billows is in agreement with the wavelength of the most dangerous mode of the stratified jet. With this theory, we also explain the weak dependence of the billows frequency with $U$. On the other hand, the stabilizing effect resulting from the combination of the proximity to a rigid boundary and stratification turns out in not observing any instabilities over the obstacle.

The experimental and simulation results show that the inclination of the jet plays a central role. In turn, the inclination is related with the flow separation. The velocity required for the separation of the jet from the surface is larger in the cylindrical obstacle than in the prismatic one. This causes the prismatic obstacle to reach regime III before the cylindrical obstacle. Although the different regimes reported in this work appear for both obstacles, the dependence of flow separation on the surface curvature makes that the critical values for passing from one regime to the other vary with the geometry of the obstacle. This shows that the structure of the

flow can change drastically when a salient edge is present at the surface of the obstacle.

We also studied the wave that propagates upstream when $F_0 > F_{0c}$, that it is predicted by hydraulic theory. In the simulations, we reproduced this wave with excellent agreement with the theory. The enhancement of the deeper layer thickness as well as the velocity of the fluid inside are in very good agreement with the theory.[1] These results indicate that the effect of this wave must be considered in flows that clearly exceed the critical conditions. For $F_0$ of the order 0.1 or less ($H_m = 0.833$, $r_0 = 0.6$), the effects of the wave may be negligible. Furthermore, the results in Figs. 7 and 8, where $F_0 < 0.1$, are not distorted in any way by the upstream effect. In the region $F_0 > 0.10$ the results remain qualitatively correct following from the comparison with numerical results. We then conclude that our experimental setup is adequate to study accurately the stratified flow for Froude numbers ranging from low values to values slightly above the critical value.

## ACKNOWLEDGMENTS

[1]P. G. Baines, *Topographic Effects in Stratified Flows* (Cambridge University Press, Cambridge, 1995).

[2]P. Baines, "A unified description of two-layer flow over topography," J. Fluid Mech. **146**, 127 (1984).

[3]W. K. Melville and K. R. Helfrich, "Transcritical two-layer flow over topography," J. Fluid Mech. **178**, 31 (1987).

[4]D. M. Farmer and L. Armi, "Stratified flow over topography: Models versus observation," Proc. R. Soc. London, Ser. A **457**, 2827 (2001).

[5]L. Armi and D. M. Farmer, "Stratified flow over topography: Bifurcation fronts and transition to uncontrolled state," Philos. Trans. R. Soc. London, Ser. A **458**, 513 (2002).

[6]G. A. Lawrence, "On the hydraulics of boussinesq and non-boussinesq two-layer flows," J. Fluid Mech. **215**, 457 (1990).

[7]G. A. Lawrence, "The hydraulics of steady two-layer flow over a fixed obstacle," J. Fluid Mech. **254**, 605 (1993).

[8]R. Dewey, D. Richmond, and C. Garrett, "Stratified tidal flow over a bump," J. Phys. Oceanogr. **35**, 1911 (2005).

[9]D. A. Aguilar and B. R. Sutherlandr, "Internal wave generation from rough topography," Phys. Fluids **30**, 066603 (2006).

[10]J. F. Scinocca and W. R. Peltier, "Pulsating downslope windstorm," J. Atmos. Sci. **46**, 2885 (1989).

[11]D. Boyer and P. Davies, "Laboratory studies of orographic effects in rotating and stratified flows," Annu. Rev. Fluid Mech. **32**, 165 (2000).

[12]D. Apsley and I. Castro, "Numerical computation of stratified flow over obstacles," in *Mixing in Geophysical Flows, International Center for Numerical Methods in Engineering*, edited by J. M. Redondo and O. Metais (Centro Internacional de Métodos, Barcelona, Spain, 1995), p. 87.

[13]G. Roden, "Effects of the fieberling seamount group upon flow and thermohaline structure in the spring of 1991," J. Geophys. Res. **99**, 9941 (1994).

[14]D. M. Farmer and L. Armi, "Stratified flow over topography: the role of small-scale entrainment and mixing in flow establishment," Philos. Trans. R. Soc. London, Ser. A **455**, 3221 (1999).

[15]C. R. Torres, A. S. Mascarenhas, Jr., and J. E. Castillo, "Three-dimensional stratified flow over Alarcón Seamount, Gulf of California entrance," Deep-Sea Res., Part I **11**, 647 (2004).

[16]P. Travassos, F. Hazin, J. Zagaglia, R. Advíncula, and J. Schober, "Thermohaline structure around seamounts and islands off North-Eastern Brazil," Arch. Fish. Mar. Res. **47**, 211 (1999).

[17]P. G. Baines and J. A. Whitehead, "On multiple states in single-layer flows," Phys. Fluids **15**, 298 (2003).

[18]L. Armi and D. M. Farmer, "Maximal two-layer exchange through a contraction with a barotropic net flow," J. Fluid Mech. **164**, 27 (1986).

[19]D. M. Farmer and L. Armi, "Maximal two-layer exchange over a sill and through the combination of a sill and contraction with a barotropic net flow," J. Fluid Mech. **164**, 53 (1986).

[20]G. Pawlak and L. Armi, "Vortex dynamics in a spatially accelerating shear layer," J. Fluid Mech. **376**, 1 (1998).

[21]J. Verron and C. LeProvost, "A numerical study of quasigeostrophic flow over isolated topography," J. Fluid Mech. **154**, 231 (1985).

[22]M. Jamali, B. Seymour, and R. Kasaiian, "Numerical and experimental study of flow of a stratified fluid over a sill towards a sink," Phys. Fluids **17**, 057106 (2005).

[23]M. Bonnier, O. Eiff, and P. Bonneton, "On the density structure of far-wake vortices in a stratified fluid," Dyn. Atmos. Oceans **31**, 117 (2000).

[24]O. S. Eiff and P. Bonneton, "Lee–wave breaking over obstacles in stratified flow," Phys. Fluids **12**, 1073 (2000).

[25]A. D. Rogers, "The biology of seamounts," Adv. Mar. Biol. **30**, 305 (1994).

[26]A. Genin, "Bio-physical coupling in the formation of zooplancton and fish aggregations over abrupt topographies," J. Mar. Syst. **50**, 3 (2004).

[27]G. N. Ivey, K. B. Winters, and J. R. Koseff, "Density stratification, turbulence, but how much mixing?" Annu. Rev. Fluid Mech. **40**, 169 (2008).

[28]J. N. Moum and J. D. Nash, "Topographically induced drag and mixing at a small bank on the continental shelf," J. Phys. Oceanogr. **30**, 2049 (2000).

[29]J. A. Carrillo, M. A. Sanchez, A. Platonov, and J. M. Redondo, "Coastal and interfacial mixing. Laboratory experiments and satellite observations," Phys. Chem. Earth, Part B **26**, 305 (2001).

[30]J. M. Klymak and M. C. Gregg, "Tidally generated turbulence over the Knight inlet sill," J. Phys. Oceanogr. **34**, 1135 (2004).

[31]P. F. Cummins, S. Vagle, L. Armi, and D. M. Farmer, "Stratified flow over topography: Upstream influence and generation of nonlinear internal waves," Philos. Trans. R. Soc. London, Ser. A **459**, 1467 (2003).

[32]D. M. Farmer and L. Armi, "The generation and trapping of solitary waves over topography," Science **283**, 188 (1999).

[33]K. G. Lamb, "On boundary-layer separation and internal wave generation at the Knight Inlet sill," Philos. Trans. R. Soc. London, Ser. A **460**, 2305 (2004).

[34]M. Stastna and W. Peltier, "On the resonant generation of large-amplitude internal solitary and solitary-like waves," J. Fluid Mech. **543**, 267 (2005).

[35]M. Stastna and W. R. Peltier, "Upstream-propagating solitary waves and forced internal-wave breaking in stratified flow over a sill," Proc. R. Soc. London, Ser. A **460**, 3159 (2004).

[36]J. Grue, "Generation, propagation, and breaking of internal solitary waves," Chaos **15**, 037110 (2005).

[37]S. Vosper, I. Castro, W. Snyder, and S. Mobbs, "Experimental studies of strongly stratified flow past three-dimensional orography," J. Fluid Mech. **390**, 223 (1999).

[38]J. Varela, M. Aaujo, I. Bove, C. Cabeza, G. Usera, A. C. Martí, R. Montagne, and L. Sarasúa, "Instabilities developed in stratified flows over pronounced obstacles," Physica A **386**, 681 (2007).

[39]G. Usera, IMFIA, Facultad de Ingeniera, J. H. Reissig 565, CP:11.300, Montevideo, Uruguay. The code is freely available for academic use through the web site (www.fing.edu.uy/imfia/caffa3d.MB) as of February 2009.

[40]Z. Lilek, S. Muzaferija, M. Peric, and V. Seidl, "Computation of unsteady flows using non-matching blocks of structured grid," Numer. Heat Transfer, Part B **32**, 403 (1997).

[41]G. Usera, A. Vernet, and J. Ferré, "Use of time resolved PIV for validating LES/DNS of the turbulent flow within a PCB enclosure model," Flow, Turbul. Combust. **77**, 77 (2006).

[42]G. Usera, A. Vernet, and J. Ferré, "A parallel block-structured finite volume method for flows in complex geometry with sliding interfaces," Flow, Turbul. Combust. **81**, 471 (2008).

[43]G. Batchelor, *An Introduction to Fluid Dynamics*, 8th ed. (Cambridge University, New York, 2007).

[44]P. Drazin and W. H. Reid, *Hydrodynamic Stability*, 2nd ed. (Cambridge University Press, Cambridge, 2004).

[45]P. Hazel, "Numerical studies of the stability of inviscid stratified flows," J. Fluid Mech. **51**, 39 (1972).